

# Image Cover Sheet

**CLASSIFICATION**

UNCLASSIFIED

**SYSTEM NUMBER**

511586



**TITLE**

Retrieval of Droplet-Size Density Distribution from Multiple-Field-of-View  
Cross-Polarized Lidar Signals: Theory and Experimental Validation

**System Number:**

**Patron Number:**

**Requester:**

**Notes:**

**DSIS Use only:**

**Deliver to:**



# Retrieval of droplet-size density distribution from multiple-field-of-view cross-polarized lidar signals: theory and experimental validation

Gilles Roy, Luc Bissonnette, Christian Bastille, and Gilles Vallée

Multiple-field-of-view (MFOV) secondary-polarization lidar signals are used to calculate the particle-size density distribution (PSD) at the base of a cloud. At the cloud base, multiple scattering is weak and single backscattering is predominant by many orders of magnitude. Because secondary polarization is a direct measure of multiple scattering, it is therefore advantageous to use secondary polarization. A mathematical relation among the PSD, the lidar fields of view, the scattering angles, and the angular depolarization is derived to facilitate use of secondary polarization. The model is supported by experimental MFOV lidar measurements carried out in a controlled environment, and its limitations and restrictions are discussed.

*OCIS codes:* 280.0280, 280.1100, 280.3640, 290.4210.

## 1. Introduction

Recent theoretical and experimental studies of multiple scattering and multiple-field-of-view (MFOV) lidar detection have made possible the retrieval of cloud droplet size.<sup>1-5</sup> Basically and as originally indicated by Eloranta<sup>6</sup> and Platt,<sup>7</sup> the enhanced lidar signal caused by multiple scattering contains information about droplet size. Multiple-scattering events are always present in clouds and are usually measured by detection of the cross-polarized component of the received signals<sup>8,9</sup> or by measurement of the lidar returns at different fields of view.<sup>10</sup> In our previous theoretical model<sup>1</sup> we used the total (sum of both polarizations) MFOV lidar signal, which limits the analysis to cloud depths large enough for multiple-scattering contributions to be significantly above the lidar pulse-to-pulse signal fluctuation. This means that droplet-size retrieval was not possible at small depths of penetration into the cloud. In this paper we show, both theoretically and experimentally, that the use of secondary polarization makes possible the retrieval of the droplet-size density function of clouds of small optical depth.

In the absence of multiple scattering, the lidar sig-

nal consists of backscattered light at exactly 180°, and a linearly polarized light source produces no secondary-polarization lidar signal because, for spherical droplets, the depolarization ratio is zero at 180°. To illustrate this, Figs. 1 and 2 show the phase function and the depolarization ratio of linearly polarized light obtained from Mie calculations for a type C2 water-droplet cloud<sup>11</sup> and a submicrometer oil-droplet suspension. The high peak values of the phase function near 0° for the water-droplet cloud are attributed to diffraction and, therefore, contain particle-size information. Diffraction does not cause depolarization, as is clearly shown in Fig. 1, but the multiple internal reflections in the water droplets cause strong depolarization at large scattering angles. The phase function and the depolarization ratio of the oil-droplet cloud are typical of Rayleigh scattering, with a signature close to a dipole (phase function quasi-flat and a zero-depolarization ratio except at 90°). As we stated above, both depolarization ratios of Figs. 1 and 2 rapidly drop to zero at exactly 180°.

## 2. Model

Basically, MFOV lidar measurements are not local measurements. They depend on the forward-scattered radiation by all aerosol particles preceding the point where the backscattering occurs. The droplet-size distribution function, particularly the number density, at the backscattering point has an effect on the amplitude of the backscatter signal but

The authors are with the Defence Research Establishment Valcartier, 2459 Pie XI Boulevard North, Val Belair, Quebec G3J 1X5, Canada. The e-mail address for G. Roy is gilles.roy@drev.dnd.ca.

Received 12 November 1998; revised manuscript received 13 April 1999.

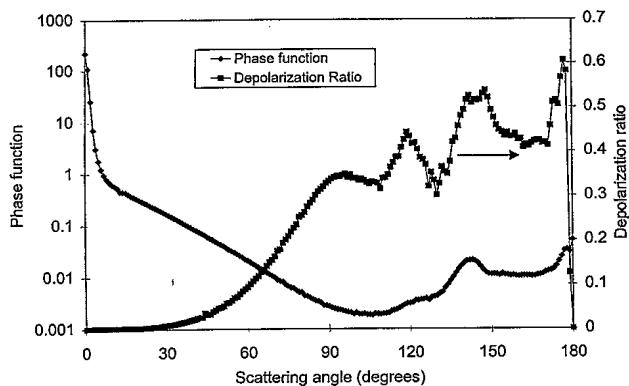


Fig. 1. Phase function and depolarization of a C2-type cloud.

has little effect on its angular spreading, as the backscattering phase function is rather flat in comparison with the forward peak from 140° to 180°. Figure 3 illustrates the scattering processes that lead to secondary polarization in the presence of multiple scattering and defines the geometry of the problem. To keep the mathematics tractable we do not consider scattering orders higher than 2 in this model, which has the effect of limiting the application of the model to small optical depth. However, the effect of higher scattering orders is discussed in Section 5 below. The cloud is located at distance  $z_a$  from the lidar, and a first forward scattering, along  $\beta$ , occurs at a distance  $z$  followed by a backscattering, along  $\pi - \beta + \theta$ ,

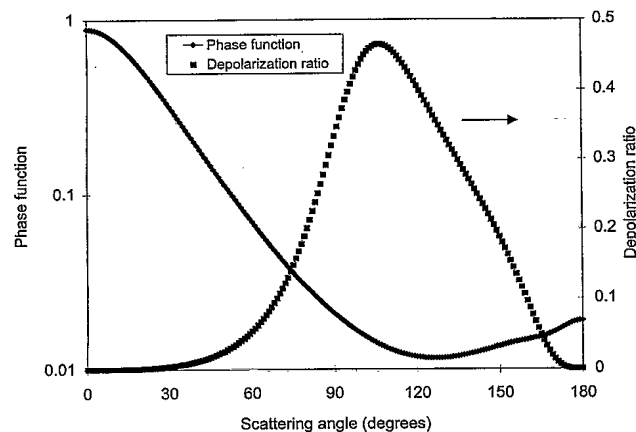


Fig. 2. Phase function and depolarization of a fog-oil cloud.

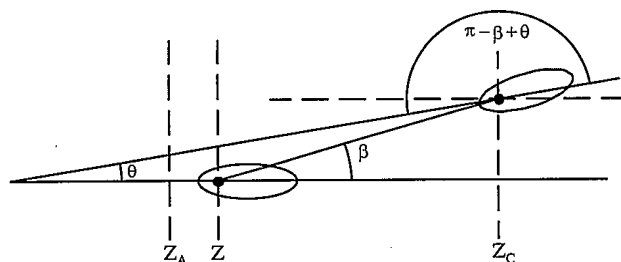


Fig. 3. Scattering processes that lead to secondary polarization.

in the plane  $z_c$ . The field of view (FOV)  $\theta$  and the scattering angle  $\beta$  are related as follows:

$$\tan \beta = \left( \frac{z_c}{z_c - z} \right) \tan \theta. \quad (1)$$

Given a cloud with extinction coefficient  $\alpha(z)$ , we obtain the measured received lidar power  $S$  in the secondary polarization between FOV's  $\theta_{j+1}$  and  $\theta_j$  by summing all the scattering contributions between distances  $z_a$  and  $z_c$  over particle-size density distribution  $q_0(x)$ , where  $x$  is the particles' diameter; i.e.,

$$S(z_c, \theta_{j+1} - \theta_j) = P_0 \exp[-2\alpha(z_c - z_a)] \frac{c\tau \rho A}{2 z_c^2} \\ \times \int_{x_{\min}}^{x_{\max}} q_0(x) \int_{z_a}^{z_c} \left[ \int_{\beta_j}^{\beta_{j+1}} x^2 I(z, x, \beta, n) \right. \\ \left. \times \sin \beta d\beta \right] \alpha(z) \delta(z, x, \langle \beta \rangle, n) dz dx, \quad (2)$$

where  $I(z, x, \beta, n)$  is the forward-scattering phase function,  $\delta(z, x, \langle \beta \rangle, n)$  is the depolarization ratio at average backscattering angle  $\pi - \langle \beta \rangle + \theta$ ,  $\langle \beta \rangle = [\beta_{j+1}(z) + \beta_j(z)]/2$ ,  $n$  is the refractive index,  $P_0$  is the laser power,  $c\tau$  is the product of the speed of light and the pulse width,  $\rho$  is the backscattering coefficient at  $z_c$ , and  $\alpha(z)$  is the scattering coefficient. The number density distribution  $q_0(x)$  can be converted to the volume density distribution<sup>12</sup>  $q_3(x)$  by means of the equation

$$q_0(x) = \frac{x^{-3} q_3(x)}{\int_{x_{\min}}^{x_{\max}} x^{-3} q_3(x) dx}, \quad (3)$$

and the integral over  $x$  in Eq. (2) is divided into  $M$  particle-size intervals with  $q_3(x)$  set equal to a constant in each interval. We thus rewrite Eq. (2) as

$$S(z_c, \Delta\theta_j) z_c^2 = \sum_{i=1}^M C_3 \bar{q}_3(\bar{x}_i) \\ \times \int_{x_i}^{x_{i+1}} \int_{z_a}^{z_c} \left[ \int_{\beta_j}^{\beta_{j+1}} x^{-1} I(z, x, \beta, n) \right. \\ \left. \times \sin \beta d\beta \right] \alpha(z) \delta(z, x, \langle \beta \rangle, n) dz dx. \quad (4)$$

Equation (4) is rewritten in matrix form as

$$\mathbf{S} = \mathbf{A} \mathbf{q}_3, \quad (5)$$

where the matrix coefficients are given by

$$A_{ij} = C_3 \int_{x_i}^{x_{i+1}} \int_{z_a}^{z_c} \left[ \int_{\beta_j}^{\beta_{j+1}} x^{-1} I(z, \beta, x, n) \sin \beta d\beta \right] \\ \times \alpha(z) \delta(z, x, \langle \beta \rangle, n) dz dx, \quad (6)$$

where  $C_3$  is a constant with respect to  $z$ ,  $x$ , and  $\beta$ .

From Eq. (5) and (6) the particle-size density distribution (PSD)  $q_3$  is obtained through matrix inversion. However, as in many inverse problems in physics, the direct inversion of Eq. (5) does not lead to satisfactory results. It is necessary to use a constrained linear inversion technique. Equation (6) contains the unknown range-dependent scattering coefficient  $\alpha(z)$ . However, because the system is not calibrated and the constant  $C_3$  is unspecified, the PSD can be determined only in relative units. Therefore we need only the relative strength of  $\alpha(z)$ . Because the method is applicable at small penetration depths, we can take  $\alpha(z)$  proportional to the measured total lidar signal.

Before considering calculations, we first need to define the depolarization  $\delta(z, x, \langle\beta\rangle, n)$ , and the forward-scattering phase function  $I(z, x, \beta, n)$ . The depolarization  $\delta(z, x, \langle\beta\rangle, n)$  is obtained<sup>13</sup> by Mie theory and is given by

$$\delta(z, x, \langle\beta\rangle, n) = \frac{P_2(\langle\beta\rangle)\cos^2(\langle\beta\rangle) - 2P_3(\langle\beta\rangle)\cos(\langle\beta\rangle) + P_1(\langle\beta\rangle)}{3P_2(\langle\beta\rangle)\cos^2(\langle\beta\rangle) + 2P_3(\langle\beta\rangle)\cos(\langle\beta\rangle) + 3P_1(\langle\beta\rangle)}, \quad (7)$$

where  $P_1$ ,  $P_2$ , and  $P_3$  are the scattered Stokes parameters.

For droplets that are significantly larger than the wavelength, the forward-scattering phase function  $I(z, x, \beta, n)$  can be obtained by use of Mie theory or the Fraunhofer diffraction theory<sup>14</sup> in conjunction with an analytical expression for the geometrical optics component.<sup>15,16</sup> Note that the agreement between the two theories is quite good for droplets larger than the wavelength and for scattering angles smaller than  $45^\circ$ . In Eq. (2) the integral over  $\beta$  corresponds to a difference of encircled energy. This difference is maximum in the region where the encircled energy function increases the most rapidly,<sup>14</sup> and the particle-size ranges in Eq. (2) are chosen in this region to yield the maximum energy difference for the diagonal matrix elements,<sup>1</sup> which helps in achievement of a robustness that naturally helps in the inversion of matrix  $\mathbf{A}$ . The Fraunhofer diffraction theory leads to an easy-to-use analytical definition of the encircled energy, and it is useful in defining the particle-size range. However, Mie theory is used here to extend the applicability of the inversion technique to droplets smaller than the wavelength.

Figure 4 shows the calculated [Eq. (4)] range-corrected  $s$ -polarization lidar return within FOV's  $\theta_i$  and  $\theta_{i+1}$  as a function  $\theta_{i+1}$  for a uniform cloud beginning at a distance of 95 m from the lidar and with a penetration depth of 6 m. The assumed water-droplet size density distributions are three log-normal distributions, with 20, 10, and 0.8  $\mu\text{m}$  as geometric mean diameters and with geometric standard deviations  $\ln\sigma = 0.2, 0.2, 0.58$ , respectively. The larger the droplet, the narrower the diffraction peak and therefore the maximum the energy col-

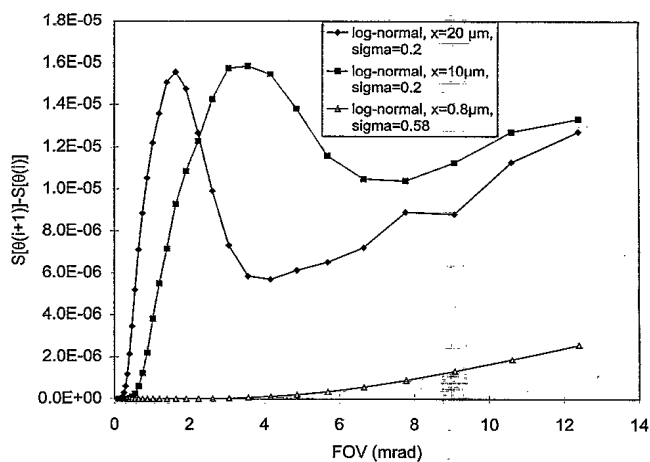


Fig. 4. Range-corrected  $s$ -polarization lidar return within FOV's  $\theta_i$  and  $\theta_{i+1}$  as a function of FOV  $\theta_{i+1}$ . The curves are for log-normal droplet-size distributions of several mean diameters and logarithmic standard deviations.

lected at small FOV's. The FOV signature is distinct and characterizes the droplet-size density distribution. Figure 5 shows the corresponding signals integrated over FOV  $\theta_{i+1}$  as a function of  $\theta_{i+1}$ . These curves give the secondary-polarization energy contained in FOV  $\theta_{i+1}$ .

### 3. Inversion

Because the direct inversion of Eq. (5) does not lead to satisfactory results it is necessary to use a constrained linear inversion technique,<sup>17,18</sup> which gives a solution of the form

$$q = (A^T A + \gamma H)^{-1} A^T P, \quad (8)$$

where  $\gamma$  is a Lagrangian multiplier and  $H$  (the second difference) is a matrix that we have used to establish a relation between successive values of  $q_i$ .

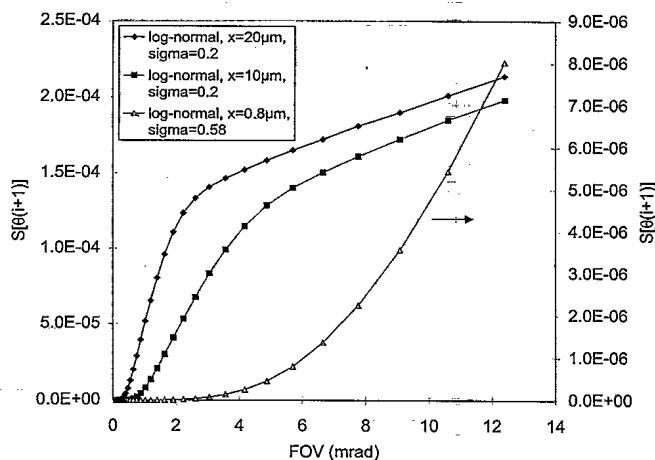


Fig. 5. Range-corrected  $s$ -polarization lidar return within FOV  $\theta_{i+1}$  as a function of FOV  $\theta_{i+1}$ .

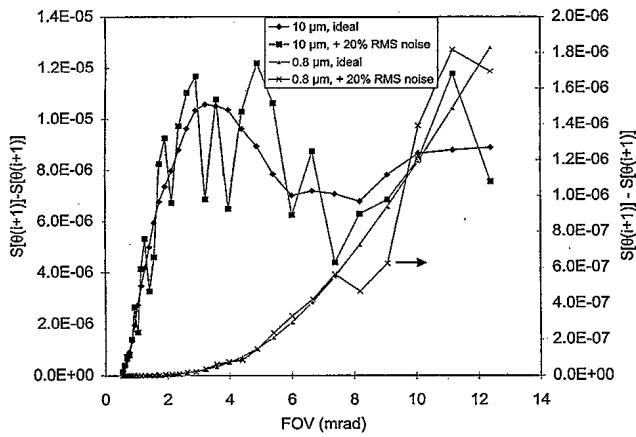


Fig. 6. Ideal lidar signals  $S(\theta_{i+1}) - S(\theta_i)$  and signals with 20% white noise as function of FOV  $\theta_{i+1}$  for a cloud made from log-normally distributed particles with median diameters of 10 and 0.8  $\mu\text{m}$ . The distance to the lidar is 95 m, and the penetration depth is 6 m.

One determines the Lagrangian multiplier of Eq. (8) by performing the inversion on synthetic MFOV lidar signals calculated for a known PSD. Typically, the range of  $\gamma$  is within the range of the product of the

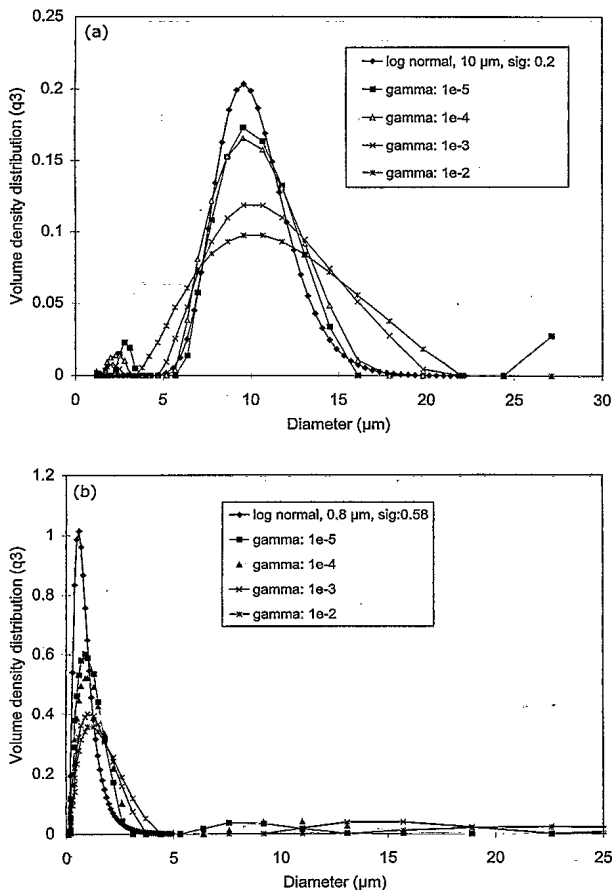


Fig. 7. Effect of  $\gamma$  on the recovery of the initial density distribution: (a)  $x_m = 10 \mu\text{m}$ , (b)  $x_m = 0.8 \mu\text{m}$ . sig, Logarithmic standard deviation.

matrix coefficients. Figure 6 shows the lidar signals  $S(\theta_{i+1}) - S(\theta_i)$  as functions of FOV  $\theta_{i+1}$  for two log-normal distributions, i.e.,

$$q_s(x) = \frac{1}{x\sigma\sqrt{2\pi}} \exp[-(\ln x - \ln x_m)^2/\sigma^2], \quad (9)$$

with  $x_m = 0.8, 10 \mu\text{m}$  and  $\sigma = 0.58, 0.2$ , respectively. The water-droplet cloud is located at a distance  $z_a$  of 95 m from the lidar. The target position is at 101 m for a penetration depth inside the cloud of 6 m. The refractive index of water is equal to (1.33, 0). In the same figure, the same  $S(\theta_{i+1}) - S(\theta_i)$  are replotted with 20% rms white noise.

Figures 7(a) and 7(b) show the particle-size volume density distributions recovered for various  $\gamma$  in the absence of noise for  $x_m = 10 \mu\text{m}$  and  $x_m = 0.8 \mu\text{m}$ , respectively. Figure 8 illustrates the effect of added noise. A  $\gamma$  of  $10^{-3}$  appears to be an acceptable value. The recovered distributions obtained for the 0.8- $\mu\text{m}$  particles are not so good as those obtained for the larger, 10- $\mu\text{m}$  particles in the absence of noise. Small particles are characterized by large scattering angles, and the inaccuracy of the inversion is likely caused by undersampling of large scattering angles. For example, less than 10% of the cloud's probed length contributes to measurements at scattering an-

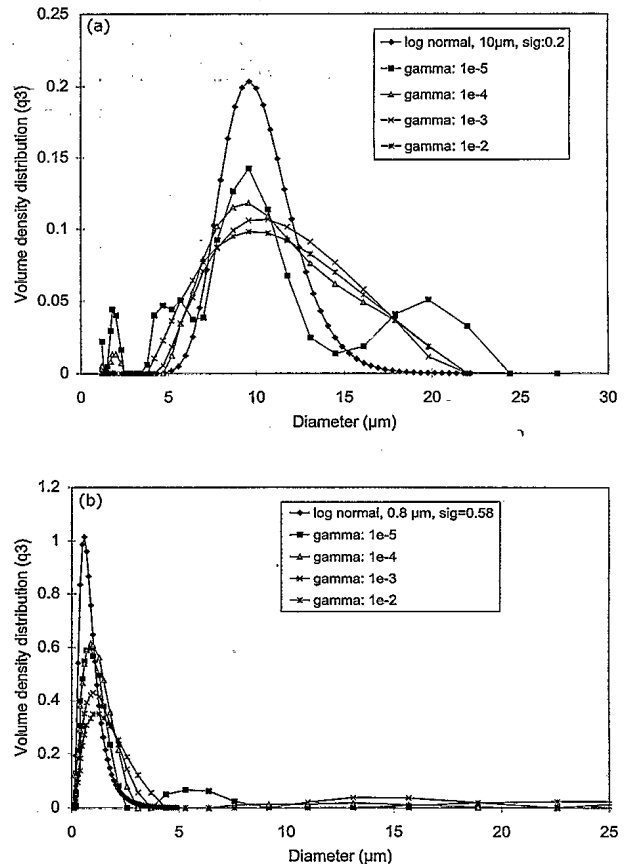


Fig. 8. Influence of noise on choice of  $\gamma$ : (a)  $x_m = 10 \mu\text{m}$ , (b)  $x_m = 0.8 \mu\text{m}$ . sig, logarithmic standard deviation.

gles greater than  $45^\circ$  for our measurements made at a 6-m penetration depth.

#### 4. Experimental Validation

MFOV lidar measurements were made under a controlled environment with a 22-m-long aerosol chamber. Two dissemination systems, distributed pneumatic water nozzles and a MDG Super Max 5000 fog-oil generator, were used to generate droplets of fairly different sizes. In the first case the generated water droplets were 10–80  $\mu\text{m}$  in diameter, in the second case the oil droplets had submicrometer diameters. The aerosol chamber was situated 95 m from the lidar. We used longitudinal and transverse transmissometers to measure the optical depth, and *in situ* particle sizing of the water droplets was performed in the middle of the chamber with a Malvern particle sizer. Figure 9 shows a typical water-droplet volume density distribution such as measured with the Malvern particle sizer. In the same figure we also show a fog-oil-droplet volume density distribution obtained from the literature<sup>19</sup> (a log-normal distribution with a geometric mean volume diameter of 0.8  $\mu\text{m}$  and a geometric standard deviation of 0.58). Fog-oil droplets are too small to be measured with the Malvern instrument.

The MFOV lidar measurements were made sequentially with a 100-Hz repetition-rate Nd:YAG laser (Kigre Workhorse Model 1732) synchronized with a rotating aluminized glass disk etched at the periphery with 32 irises or rings of different apertures, as illustrated in Fig. 10. The ring-mask measurements have the advantage of being less sensitive to shot-to-shot cloud fluctuations. However, the small area of the inner rings make the individual measurements fall below the detection threshold quickly with increasing optical depth and thus lead to invalid cumulative measurements. Table 1 lists the individual rings' inner and outer diameters. The diameters of the iris masks are identical to the outer diameters of the ring masks. Both disks are mounted in the im-

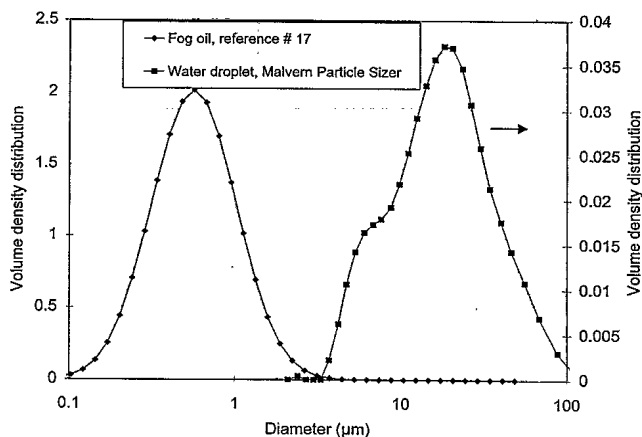


Fig. 9. Volume density distributions of a generated water-droplet cloud measured with a Malvern Particle Sizer and of typical published values for fog-oil clouds.<sup>17</sup>

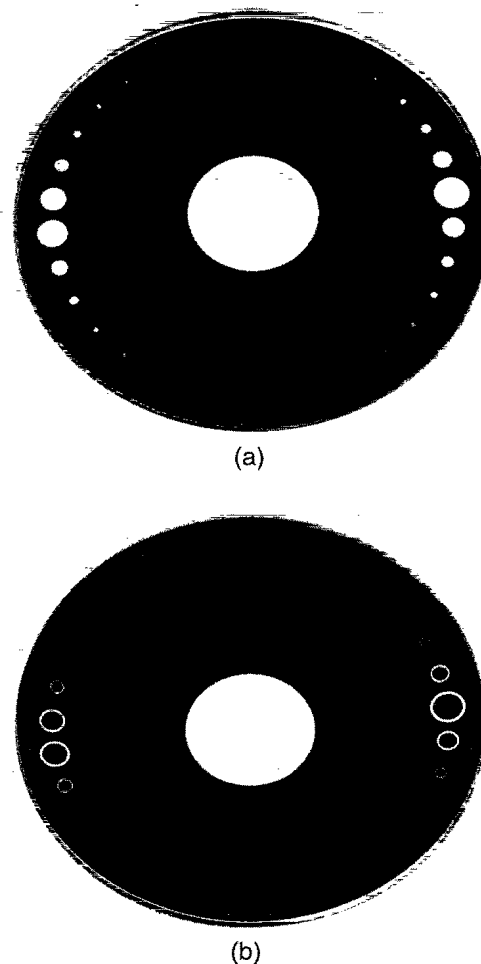


Fig. 10. Aluminized glass plate with 32 etched irises. (a) The order of the irises was set to cover the maximum FOV difference within 1/4 of a turn. (b) The order of the rings is the same as for the irises.

age plane of the primary optics, as illustrated in Fig. 11. The primary optics consists of a 200-mm-diameter off-axis parabolic mirror with a focal length of 760 mm. The position of the image plane is a function of the focal length and the object position, and it is necessary to adjust the image plane position in accordance with the cloud distance. Secondary optics and a polarizer cube are used to split and re-image the two polarization components on 3-mm-diameter avalanche photodiodes (APD's). We calibrated the radial responses of the APD detectors by scanning the laser spot on a canvas target. The glass disk turns at a stabilized speed of 3.125 rotations/s, and an electronic delay was set between the synchronization holes and the laser trigger. In this configuration the laser is slaved to the FOV controller. FOV's ranging from 0.1 to 12 mrad were thus changed at a repetition rate of 100 Hz. Finally, the characteristics of the laser beam were as follows: 2.5-cm diameter and 0.3-mrad divergence (50% total energy), linear polarization purity of 1/500 ensured with a high-power polarizer cube, an outgoing energy

Table 1. Inner and Outer Ring Diameters Etched on the Rotating Glass Disk

Ring Number	Inner Ring Diameter ( $\mu\text{m}$ )	Outer Ring Diameter ( $\mu\text{m}$ )
1	0	76
2	76	89
3	89	104
4	104	121
5	121	142
6	142	165
7	165	193
8	193	226
9	226	264
10	264	308
11	308	360
12	360	420
13	420	491
14	491	574
15	574	670
16	670	783
17	783	915
18	915	1069
19	1069	1249
20	1249	1458
21	1458	1704
22	1704	1990
23	1990	2326
24	2326	2716
25	2716	3174
26	3174	3707
27	3707	4331
28	4331	5059
29	5059	5911
30	5911	6905
31	6905	8064
32	8064	9424

Table 2. Trial List Parameters

Trial Number and Medium	Penetration Depth (m)	Optical Depth	FOV Type
pvri0318, water	6	0.4	Ring
pvh0305, water	6	0.2	Iris
pvh0305, water	10	0.4	Iris
fori0308, oil	6	0.4	Ring
foh0308, oil	6	0.4	Iris

per pulse in the atmosphere of 60 mJ, and a pulse width of 12 ns.

The measurements were usually performed early in the morning so the relative humidity was high and the wind mild. Table 2 lists four trials that we used

to demonstrate the PSD lidar polarization technique. Figure 12 shows the water-droplet trial number pvri0318 principal *p*- and secondary *s*-polarization lidar returns as functions of distance for two total FOV's. For this representation the individual ring signals are summed to 0.75 and 12 mrad, respectively. In Fig. 13 we display the corresponding signals for oil-droplet trial number foh0301. Clearly at the beginning of each cloud the *p*-polarization measurement values are 2–3 orders of magnitude higher than the *s*-polarization values. Without polarization separation, the multiple-scattering signal would be lost in the main polarization signal fluctuations. For the large water droplets, the differences between the two FOV signals increase with distance (optical depth), whereas for the small oil droplets the differences remain quasi-constant, as is particularly evident for *s* polarization.

Figures 14 and 15 show the measured secondary *s*-polarization ring and cumulative signals, respectively, as functions of FOV  $\theta_{j+1}$  at a distance of 101 m (i.e., 6 m into the cloud) for the water- and fog oil droplet clouds. Figure 16 shows the cumulative measurements obtained for trials pvh0305 and foh0301 at distances of 101 and 105 m (i.e., 6 and 10 m into the cloud). The profiles of Figs. 14–16 are multiple-scattering measurements and show trends comparable to those of the model-based calculated signals plotted in Figs. 4 and 5. To better illustrate the effect of multiple scattering, we added to Fig. 15

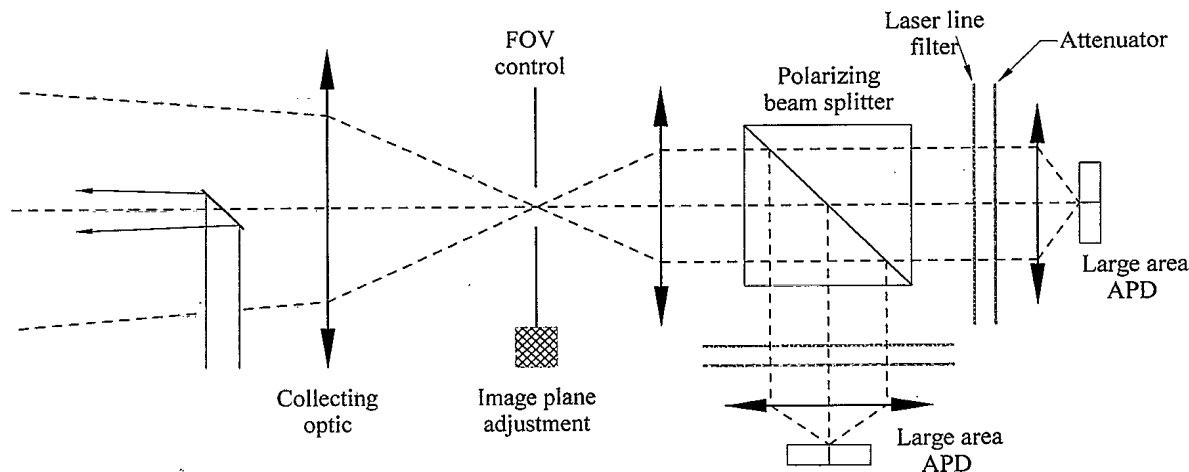


Fig. 11. Setup for the detection module used for sequential MFOV lidar measurements. FOV control is basically the ring or iris rotating dish assembly mounted on a precision translator.



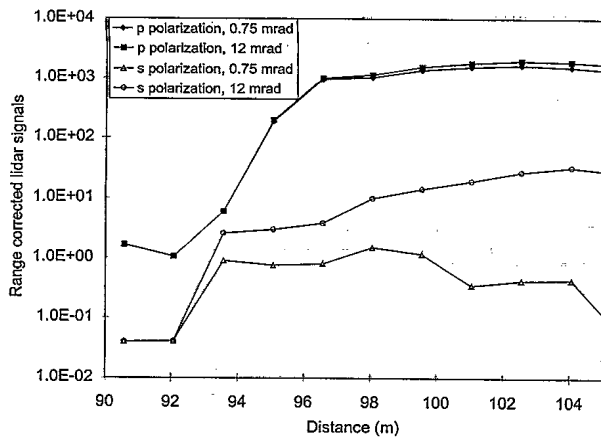


Fig. 12. Range-corrected lidar return *p*- and secondary *s*-polarization lidar return as functions of distance for 0.75- and 12-mrad total FOV's for water droplet trial pvri0318.

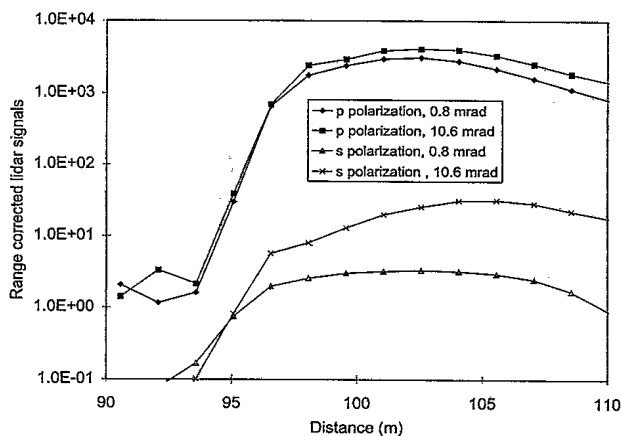


Fig. 13. Range-corrected lidar return *p*- and secondary *s*-polarization lidar return as functions of distance for 0.75- and 12-mrad total FOV's for the fog-oil trial foh0301.

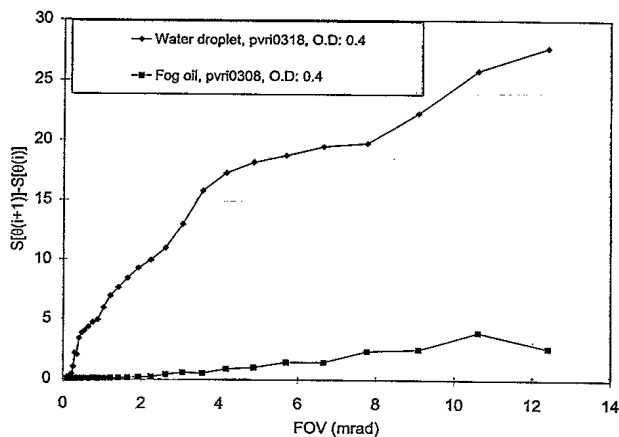


Fig. 14. Range-corrected *s*-polarization lidar return within FOV's  $\theta_i$  and  $\theta_{i+1}$  as a function of FOV  $\theta_{i+1}$  for a distance of 101 m (penetration depth of 6 m) and an optical depth (O.D.) of 0.4.

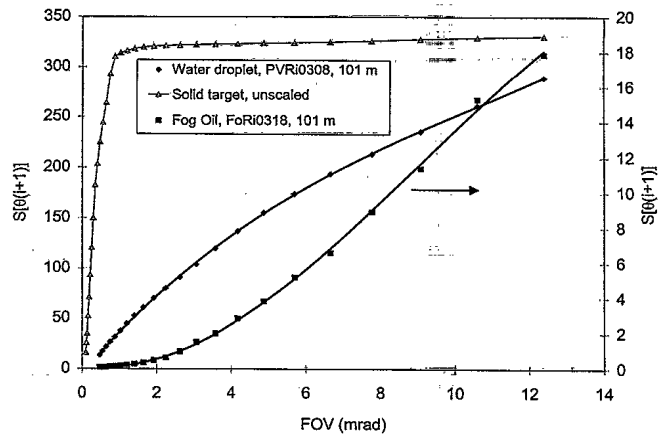


Fig. 15. Range-corrected *s*-polarization lidar return within FOV  $\theta_{i+1}$  as a function of FOV  $\theta_{i+1}$  for a distance of 101 m (penetration depth of 6 m) and an optical depth of 0.4. The lidar return from a solid target located at a distance of 200 m is also plotted.

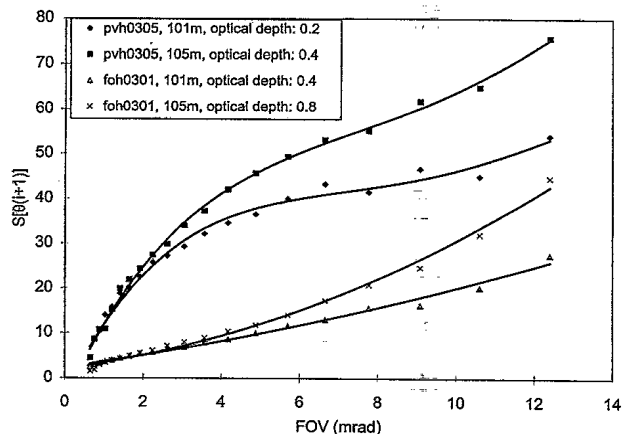


Fig. 16. Range-corrected *s*-polarization lidar return within  $\theta_{i+1}$  as a function of FOV  $\theta_{i+1}$  for distances of 101 and 105 m (penetration depths of 6 and 10 m) and optical depths of 0.2, 0.4, and 0.8.

the unscaled lidar signal obtained from a solid target; in this case there is no multiple scattering, and the displayed signal is the laser footprint with no artifact.

We use the *s*-polarization measurements to generate the **S** vector of Eq. (5), and the matrix elements are calculated with Eq. (6). The particle-size volume density distributions **q**<sub>3</sub> are then obtained through the matrix inversion of Eq. (5) by a conventional second-difference constrained linear inversion technique. Figure 17 shows the retrieved **q**<sub>3</sub> for the two water-droplet trials as well as a typical Malvern particle sizer result. The results from trial number pvh0305 at optical depths of 0.2 and 0.4 match the Malvern result fairly well. However, the results from trial pvri0318 show droplets definitely smaller than the Malvern result. Figure 18 compares the retrieved **q**<sub>3</sub> obtained for the fog-oil-droplet measurements with the result obtained from the literature.<sup>19</sup> Also plotted in the same figure is the retrieved **q**<sub>3</sub> from synthetic data generated with the original PSD

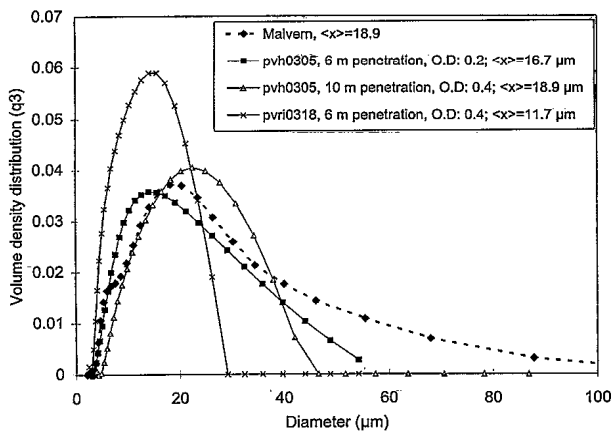


Fig. 17. Comparison of particle-size density distributions obtained in two trials by application of matrix inversion to secondary-polarization MFOV measurements from water-droplet clouds with measurements made with the Malvern particle sizer. O.D., optical depth.

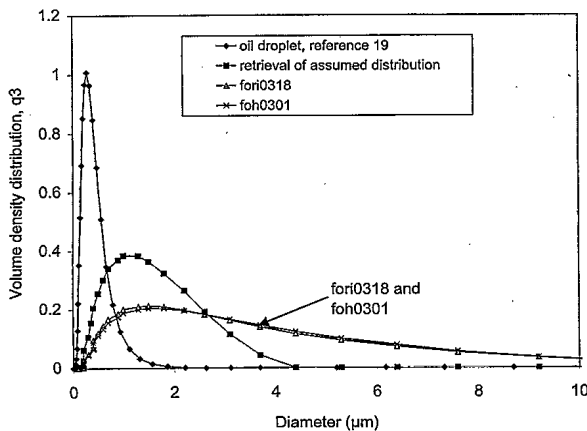


Fig. 18. Comparison of the particle-size density distribution obtained by application of matrix inversion to the secondary-polarization MFOV measurements from fog-oil cloud with a published<sup>19</sup> distribution.

from the literature. As we pointed out in Section 3, the inversion technique does not retrieve the initial distribution well for small particles; the density distribution is broadened and shifted toward larger particles. Therefore it is not surprising that the  $q_3$  retrieved from experimental data shows larger particles than the values reported in the literature. But

it is evident that the measured distributions are significantly wider than the assumed distribution, indicating that the actual oil droplets for the smoke generator are larger than those reported in the literature. To quantify the agreement-disagreement between the reported density distributions of Figs. 17 and 18 we list in Table 3 the mean diameters calculated from the retrieved distributions. We transformed volume density distribution  $q_3$  into number density distribution  $q_0$  to calculate the mean particle diameter and the surface-volume mean diameter (the Malvern and literature values are given in parentheses). For measurements pvh0305, the agreement is fairly good between the s-polarization lidar results performed at 6- and 10-m penetration depths (optical depths of 0.2 and 0.4) and those obtained with the Malvern particle sizer. However, as we pointed out above, measurements pvri0318 at the entrance of the aerosol chamber, i.e., at a penetration of 6 m, lead to smaller droplets than those obtained at the middle of the chamber (lidar at 105 m and the Malvern instrument). This difference is probably caused by the evaporation of the water droplets in contact with the dryer outdoor air; the relative outdoor humidity went down to 60% for this particular trial. The results obtained for the fog oil are in agreement within a factor of 2–3 with those obtained from the literature. This is a good result, as we know that the literature values do not consider a specific fog-oil generator and that the inversion technique is less accurate for particles smaller than the probing wavelength. Small particles are characterized by large scattering angles, and the inaccuracy of the inversion is possibly caused by undersampling of large scattering angles. For example, less than 10% of the cloud's probed length contributes to measurements at scattering angles greater than  $45^\circ$  for our measurements made at a 6-m penetration depth.

### 5. Limitation of Present Model

In Section 1 we pointed out that our model is restricted to small optical depths, so first-order forward scattering is predominant. To quantify the small optical depth restriction, we estimate the relative contributions of the different scattering orders as functions of optical depth. We proceed as in Ref. 1 and use an extension of the Beer-Lambert law. Given  $I_0$ , the incident intensity on a homogeneous cloud, the unscattered intensity loss and the amount

Table 3. Comparison of the Measured Mean Values<sup>a</sup>

Trial Number	Penetration Depth (m)	Optical Depth	$\langle x \rangle q_3$ ( $\mu\text{m}$ )	$\langle x \rangle q_0$ ( $\mu\text{m}$ )	$\langle x^3 \rangle q_0 / \langle x^2 \rangle q_0$ ( $\mu\text{m}$ )	$x_{\text{max}}$ ( $\mu\text{m}$ )
pvri0318	6	0.4	14.4 (28.8)	6.9 (8.2)	11.7 (18.9)	14.9 (17.3)
pvh0305	6	0.2	22.5 (28.8)	8.5 (8.2)	16.7 (18.9)	15 (17.3)
pvh0305	10	0.4	23.8 (28.8)	11.6 (8.2)	19.6 (18.9)	22.6 (17.3)
fori0308	6	0.4	2.5 (1)	0.3 (0.3)	1.4 (0.67)	1.2 (0.8)
foh0301	6	0.4	2.4 (1)	0.3 (0.3)	1.4 (0.67)	1.2 (0.8)

<sup>a</sup>The values in parentheses were obtained with the Malvern Particle Sizer or from the literature.

of scattered intensity as functions of penetration depth obey the Beer-Lambert law, i.e.,

$$I_T = I_0 \exp(-\alpha z), \quad (10)$$

$$I_{D1} = I_0 [1 - \exp(-\alpha z)], \quad (11)$$

where  $I_T$  is the transmitted intensity and  $I_{D1}$  is the scattered intensity. Part of the scattered intensity is rescattered and the process is repeated for the higher scattering orders. In the small-angle scattering approximation (predominance of forward scattering), the transmission loss of the doubly scattered beam can be approximated by

$$\Delta I_{TD1} = -I_{TD1} [1 - \exp(-\alpha z)] \alpha \Delta z, \quad (12)$$

and the solution is

$$I_{TD1} = I_0 \exp(-\alpha z) \{\exp[1 - \exp(-\alpha z)]\}, \quad (13)$$

$$I_{D2} = I_0 [1 - \exp(-\alpha z) \{\exp[1 - \exp(-\alpha z)]\}], \quad (14)$$

where  $I_{TD1}$  is the fraction of the scattered beam ( $I_{D1}$ ) that is transmitted and  $I_{D2}$  is the fraction that is rediffused. Proceeding in the same way to third order, we find that

$$I_{TD2} = I_0 \exp(-\alpha z - 1) \exp\{\exp[1 - \exp(-\alpha z)]\}, \quad (15)$$

$$I_{D3} = I_0 (1 - \exp(-\alpha z - 1) \exp\{\exp[1 - \exp(-\alpha z)]\}), \quad (16)$$

where  $I_{TD2}$  is the fraction of the scattered intensity  $I_{D2}$  that is transmitted and  $I_{D3}$  is the fraction that is rediffused. Finally, the transmission loss to fourth order is written as

$$I_{TD3} = I_0 \exp \left[ - \int I_{D3} \alpha(z) dz \right], \quad (17)$$

$$I_{D4} = I_0 (1 - I_{TD3}), \quad (18)$$

where  $I_{TD3}$  is the fraction of the scattered intensity  $I_{D3}$  that is transmitted and  $I_{D4}$  is the fraction that is rediffused.

Figure 19 shows the relative contributions of the

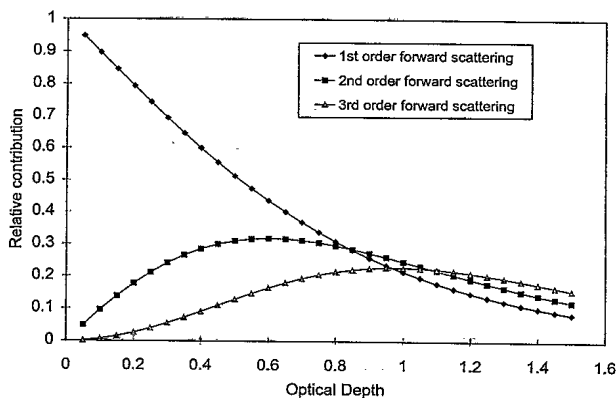


Fig. 19. Approximate relative lidar contributions of the three scattering orders as functions of apparent optical depth.

various scattering orders ( $I_{D,i-1} - I_{D,i}$ ) normalized with scattered intensity  $I_{D1}$  as functions of the optical depth divided by 2. These expressions model the relative contributions by higher-order forward scattering to lidar returns in the approximation that backscatter sensitivity to scattering order is slight. The division by 2 is necessary because in lidar geometry the two-way transmission through the scattering medium has to be considered. The higher scattering orders successively become predominant as optical depth increases. Clearly, the contributions of second-order forward scattering cannot be neglected for optical depths greater than 0.3–0.4. The effects of higher forward-scattering orders are to spread the scattered photons at larger angles and also to redirect energy back into the inner FOV's, making the relationship given by Eq. (1) between the scattering angle and the FOV invalid. How is this extra energy interpreted by the present model? Can the higher scattering orders be properly modeled? These are questions outside the scope of this paper, but they must be answered if the PSD retrieval from lidar secondary polarization is to be expanded to optical depths greater than 0.4.

The particle-size resolution is range and size dependent. The resolution of large particles requires small FOV's, and those FOV's have to be even smaller when the cloud is situated at a greater distance from the lidar. Small FOV's lead to the following requirements or restrictions:

The FOV ring-iris mask disk must be positioned in the image plane of the principal optics. To cover cloud near and far distances and maintain FOV precision it is necessary to adjust the image plane position with a translation stage.

Ideally the laser spot size on the cloud should subtend an angle smaller than the smallest FOV. This means that outgoing laser beam size and divergence smaller than 25 mm and 0.1 mrad, respectively, are required.

The transmitter and receiver optics has to be colinear, and the alignment must be maintained within the smallest FOV.

## 6. Conclusion

The proposed technique based on the use of the secondary polarization offers good potential for the determination of the PSD of clouds. The advantage is that the useful multiple-scattering signal is not buried under strong single-scattering contributions. The proposed method is applicable at small penetration depths, but this is the very region where it is useful, i.e., where it is difficult to separate multiple from single-scattering contributions in conventional total return measurements. The present method is applicable only at small penetration depths and does not require absolute knowledge of extinction coefficient  $\alpha(z)$ , which is set proportional to the measured total lidar signal. The model is relatively simple in application, and the measurements are easily done with FOV segmentation. The measurements require low laser beam divergence, small laser beam

size, and imaging-quality collection optics. The technique can be applied for particle sizing of large spray-nozzle systems, stack emissions, and thin natural clouds. Finally, because the technique uses a unique characteristic of spherical droplets, i.e., zero depolarization at  $180^\circ$ , it cannot be readily applied to nonspherical particles or to large droplets that are frequently found to be oblate.

## References

1. G. Roy, L. C. Bissonnette, C. Bastille, and G. Vallée, "Estimation of cloud droplet size density distribution from multiple-field-of-view lidar returns," *Opt. Eng.* **36**, 3404–3415 (1997).
2. L. R. Bissonnette, "Multiple-scattering lidar equation," *Appl. Opt.* **35**, 6449–6465 (1996).
3. L. R. Bissonnette and D. L. Hutt, "Multiply scattered aerosol lidar returns: inversion method and comparison with *in situ* measurements," *Appl. Opt.* **34**, 6959–6975 (1995).
4. Y. Benayahu, A. Ben-David, S. Fastig, and A. Cohen, "Cloud-droplet-size distribution from lidar multiple-scattering measurements," *Appl. Opt.* **34**, 1569–1578 (1995).
5. E. W. Eloranta, "Practical model for the calculation of multiply scattered lidar returns," *Appl. Opt.* **37**, 2464–2472 (1998).
6. E. W. Eloranta, "Calculation of doubly scattered lidar returns," Ph.D. dissertation (University of Wisconsin, Madison, Wisc., 1972).
7. C. M. R. Platt, "Lidar and radiometer observations of cirrus clouds," *J. Atmos. Sci.* **30**, 1191–1204 (1973).
8. R. J. Allen and C. M. R. Platt, "Lidar for multiple backscattering and depolarization observation," *Appl. Opt.* **16**, 3193–3199 (1977).
9. S. R. Pal and A. I. Carswell, "Polarization properties of lidar scattering from clouds at 347 nm and 694 nm," *Appl. Opt.* **17**, 2321–2328 (1978).
10. K. Sassen and R. L. Petrilla, "Lidar depolarization from multiple scattering in marine stratus clouds," *Appl. Opt.* **25**, 1450–1459 (1986).
11. E. P. Shettle, "Models of aerosols, clouds and precipitation for atmospheric propagation studies," in *Atmospheric Propagation in the UV, Visible, IR and MM-Wave Region and Related System Aspects*, AGARD Conf. Proc. **454**, 1–5 (1989), paper 15.
12. T. Allen, *Particle Size Measurement* (Chapman & Hall, New York, 1981).
13. K. Sassen and H. Zhao, "Lidar multiple scattering in water droplet clouds: toward an improved treatment," *Opt. Rev.* **2**, 394–400 (1995).
14. M. Born and E. Wolf, *Principles of Optics* (Pergamon, New York, 1975).
15. J. R. Hodkinson and J. Greenleaves, "Computations of light-scattering and extinction by spheres according to diffraction and geometrical optics, and some comparisons with Mie theory," *J. Opt. Soc. Am.* **53**, 577–582 (1963).
16. M. Kerker, *The Scattering of Light and Other Electromagnetic Radiation* (Academic, New York, 1969).
17. S. Twomey, *Introduction to the Mathematics of Inversion in Remote Sensing and Indirect Measurements* (Elsevier, Amsterdam, 1977).
18. M. Heuner and K. Leschonski, "Results obtained with a new instrument for the measurement of particle size distributions from diffraction patterns," *Part. Part. Syst. Charact.* **2**, 7–13 (1985).
19. D. H. Pollock, *Countermeasure Systems*, Vol. 7 of *The Infrared & Electro-Optical Systems Handbook* (Environmental Research Institute of Michigan, Ann Arbor, Mich., 1993).

#51386